

Electronic Structure of the Bond Disproportionated Bismuthate Ag_2BiO_3

Mohamed Oudah^{1,2,*}, Minu Kim¹, Ksenia S. Rabinovich¹, Kateryna Foyevtsova², Graham McNally¹, Berkay Kilic¹, Kathrin Küster¹, Robert Green^{2,3}, Alexander V. Boris¹, George Sawatzky², Andreas P. Schnyder¹, D. A. Bonn², Bernhard Keimer¹, and Hidenori Takagi^{1,4}

¹Max Planck Institute for Solid State Research, Heisenbergstrasse 1, 70569 Stuttgart, Germany

²Stewart Blusson Quantum Matter Institute, University of British Columbia, Vancouver, British Columbia V6T 1Z4, Canada

³Department of Physics & Engineering Physics, University of Saskatchewan, Saskatoon, Saskatchewan S7N 5E2, Canada

⁴Department of Physics, University of Tokyo, Bunkyo-ku, Hongo 7-3-1, Tokyo 113-0033, Japan

(Dated: June 18, 2021)

We present a comprehensive study on the silver bismuthate Ag_2BiO_3 , synthesized under high-pressure high-temperature conditions, which has been the subject of recent theoretical work on topologically complex electronic states. We present X-ray photoelectron spectroscopy results showing two different bismuth states, and X-ray absorption spectroscopy results on the oxygen K -edge showing holes in the oxygen bands. These results support a bond disproportionated state with holes on the oxygen atoms for Ag_2BiO_3 . We estimate a band gap of ~ 1.25 eV for Ag_2BiO_3 from optical conductivity measurements, which matches the band gap in density functional calculations of the electronic band structure in the non-symmorphic space group $Pnn2$, which supports two inequivalent Bi sites. In our band structure calculations the disproportionated Ag_2BiO_3 is expected to host Weyl nodal chains, one of which is located ~ 0.5 eV below the Fermi level. Furthermore, we highlight similarities between Ag_2BiO_3 and the well-known disproportionated bismuthate BaBiO_3 , including breathing phonon modes with similar energy. In both compounds hybridization of Bi-6s and O-2p atomic orbitals is important in shaping the band structure, but in contrast to the Ba-5p in BaBiO_3 , the Ag-4d bands in Ag_2BiO_3 extend up to the Fermi level.

I. INTRODUCTION

Transition-metal oxides include many novel classes of materials that host a wide range of structures and electronic properties. The field of condensed matter physics had made a great leap forward with the discovery of high transition temperature superconductivity (T_c) in the layered copper oxides [1] and in the hole-doped cubic bismuthate (Ba,K)BiO₃ [2]. The undoped BaBiO₃ is a disproportionated insulator. Also, oxide materials have shown promise for exploring topological properties [3–5]. We identified the silver bismuthates as a promising set of materials for studying highly correlated electron systems and for finding topologically non-trivial oxides. Ag_2BiO_3 was recently highlighted in theoretical work with various predictions of topologically protected states [6–8].

The previous experimental work on Ag_2BiO_3 has resulted in a number of crystal structures reported in the Inorganic Crystal Structure Database (ICSD), which fall into the space groups $Pnna$, $Pnn2$, and Pn [9, 10]. $Pnna$ is the oldest structure reported, which has a single bismuth site implying a uniform 4+ state for bismuth and as a result equal Bi-O distances. A Bi⁴⁺ state is unusual, however, and typically a compound with nominal charge of 4+ on bismuth disproportionates. The disproportionation in BaBiO₃ is reflected in the existence of two distinct sites for Bi, but the nature of this disproportionation is debated. It was emphasized in a following neutron diffraction study that Ag_2BiO_3 has two

distinct bismuth sites and crystalizes in the $Pnn2$ space group [10], and the two sites were explained with the disproportionation of Bi⁴⁺ into Bi³⁺ and Bi⁵⁺ states. The existence of two distinct bismuth sites in Ag_2BiO_3 ($Pnn2$) is similar to BaBiO₃, but these compounds crystallize in different crystal structures, with a combination of corner- and edge-sharing BiO₆ octahedra in Ag_2BiO_3 and only corner-sharing BiO₆ octahedra in the perovskite BaBiO₃. By thoroughly characterizing the disproportionated state in Ag_2BiO_3 and comparison to BaBiO₃, we establish $(M^{1+})_2\text{BiO}_3$ as a new class of disproportionated bismuthates beyond those forming in the perovskite structure.

The disproportionation of the Bi site and resulting $Pnn2$ symmetry also have important ramifications for the topological nature of Ag_2BiO_3 . Theoretical predictions of topological phases in Ag_2BiO_3 include an hourglass nodal net semimetal [7], a Dirac semimetal [6], and an hourglass Dirac semimetal [8]. All of these topological predictions were made on Ag_2BiO_3 in the $Pnna$ phase with a single bismuth site, where breaking Bi charge order to attain the $Pnna$ symmetry is important to realizing these topologically nontrivial phases. However, we will show that Ag_2BiO_3 crystallizes in the $Pnn2$ space group with two crystallographically distinct bismuth sites even when synthesized under high-pressure and high-temperature conditions. The topological predictions made for the $Pnna$ phase therefore do not apply to Ag_2BiO_3 crystallizing in the $Pnn2$ phase. Rather, we predict Weyl states in the $Pnn2$ phase.

In this paper, we characterize Ag_2BiO_3 samples synthesized at 6 GPa using powder X-ray diffraction (XRD) and various spectroscopic techniques. We present evi-

*Electronic address: mohamed.oudah@ubc.ca

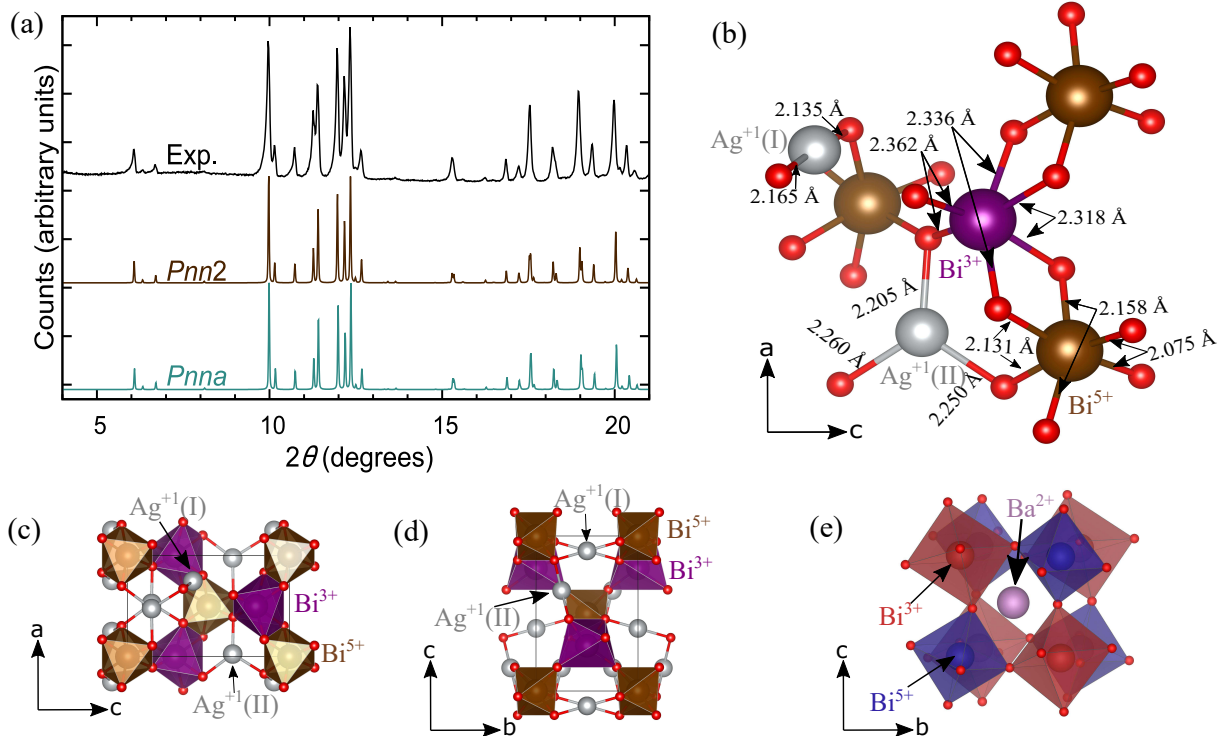


FIG. 1: (a) The powder X-ray diffraction pattern measured at room temperature of Ag_2BiO_3 (top) and the calculated pattern for Ag_2BiO_3 in the $Pnn2$ phase (middle) and the $Pnna$ phase (bottom). (b) Part of the unit cell of Ag_2BiO_3 in the $Pnn2$ phase with “ Bi^{3+} ” (purple) and “ Bi^{5+} ” (brown) highlighting the different oxygen metal distances [10]. (c) Unit cell of Ag_2BiO_3 in the $Pnn2$ phase along the ac -plane showing the shared edges of the octahedra along the a direction. (d) Unit cell of Ag_2BiO_3 in the $Pnn2$ phase along the bc -plane. (e) Unit cell of $BaBiO_3$ showing the corner-sharing octahedra and “ Bi^{3+} ” (red) and “ Bi^{5+} ” (blue).

dence from X-ray photoelectron Spectroscopy (XPS) supporting the disproportionation of bismuth into two sites in Ag_2BiO_3 , and present evidence for a bulk band gap, a consequence of the disproportionation, seen in an optical conductivity measurement. The optical gap is consistent with density functional theory (DFT) calculations of the electronic band structure in the $Pnn2$ (disproportionated) phase of this material. Our calculations, on the experimentally realized $Pnn2$ phase, further predict Weyl nodal chains (i.e., chains of connected loop degeneracies in momentum space) at various energies in this phase, one being ~ 0.5 eV below the Fermi level. We provide evidence for oxygen holes using X-ray absorption spectroscopy (XAS), and considering the XPS results we propose that Ag_2BiO_3 is bond disproportionated rather than charge disproportionated. We then highlight the extent of similarities between Ag_2BiO_3 and $BaBiO_3$; similar breathing mode peaks are observed in Raman spectra and we identify similarities in the band structure of these compounds when considering the oxygen molecular orbitals in these disproportionated bismuthates. Finally, we present new evidence from Raman spectra and XRD for the previously reported structural transition to a Pn phase at low temperature [10].

II. EXPERIMENTAL DETAILS

Ag_2BiO_3 samples were synthesized with a high-pressure, high-temperature method utilizing a belt-press. Bi_2O_3 and AgO powders were well mixed in a mortar and pestle, then loaded into a gold capsule with a drop of KOH to speed up the reaction. The capsule was then pressed to 6 GPa and heated at 730 K for 1 hour before quenching and retrieving the polycrystalline product. A finely ground sample was loaded into a 0.3 mm capillary, and powder XRD patterns of Ag_2BiO_3 were collected while rotating the capillary using Ag radiation (0.5594 \AA). The samples were cooled down to ~ 200 K for low temperature XRD.

X-ray absorption spectra of the oxygen K -edges were recorded in partial fluorescence yield (PFY) mode at the Spherical Grating Monochromator (SGM) beamline at the Canadian Light Source. Spectra in PFY mode are collected using energy resolving silicon drift detectors, which allow selection of only the oxygen K -edge fluorescence. The average of data from four separate silicon drift detectors was used for the PFY spectra. Spectra are calibrated in energy by using a TiO_2 reference sample [12]. Spectra were then normalized by the incident beam inten-

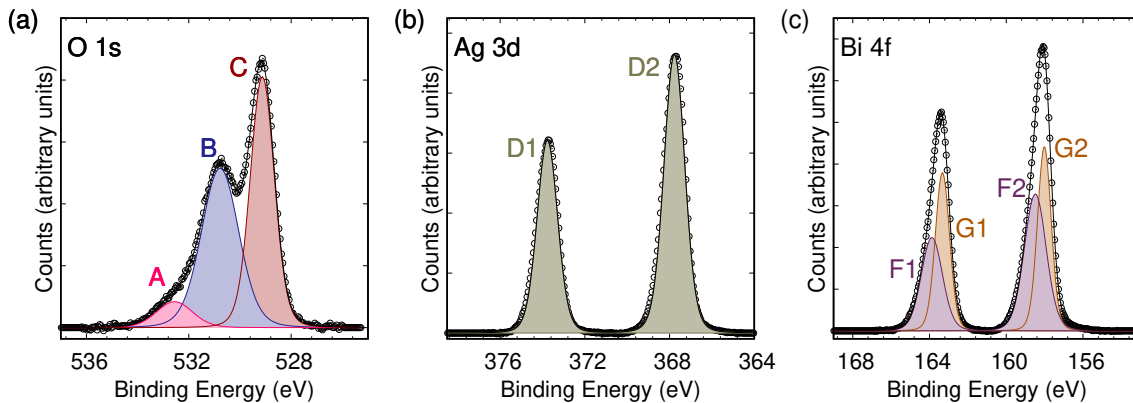


FIG. 2: X-ray photoelectron spectra of O, Ag, and Bi in Ag_2BiO_3 are shown in (a), (b), and (c). In (a) the three peaks A, B, and C are needed to fit the measured spectra for the O-1s states. In (b) the splitting between peaks D1 and D2 is consistent with that expected due to spin-orbit-coupling (SOC) for Ag-3d states. In (c) the splitting between F1 and F2 is consistent with that expected due to SOC for Bi-4f states, and the same can be said for the split between G1 and G2. Due to the asymmetry of the measured spectra, four curves are needed to fit the Bi-4f states. This leads us to conclude the existence of two different Bi states in Ag_2BiO_3 , both close in energy to Bi^{3+} [11].

sity, and normalized according to post-edge intensity after subtracting a linear background. The Ag_2BiO_3 spectra were collected under ultrahigh vacuum at room temperature from a pressed pellet attached to carbon tape, with the pellet surface at an angle of 45° to the incident beam. The XPS data were collected using a commercial Kratos AXIS Ultra spectrometer and a monochromatized Al K_α source (photon energy: 1486.6 eV). The base pressure during XPS was in the low 10^{-10} mbar range. The spectra were collected using an analyzer pass energy of 20 eV. XPS spectra were analyzed using the CasaXPS software. The charge-neutralizer was used and the C 1s was set to 284.8 eV for binding energy calibration [13, 14]. To fit the peaks, a combination of multiple Gaussian-Lorentzian mixture functions and a Shirley background was used. The binding energy separation and the area ratio of the doublets were not constrained but the results are within experimental error of the tabulated values [15]. The sum of all the fitted functions to XPS peaks is shown with a black curve in Fig. 2.

Optical spectroscopic ellipsometry measurements were performed using a variable-angle spectroscopic ellipsometer (VASE, Woollam) with photon energy in the range of 0.7–6.5 eV at incident angles of 70° . The real and imaginary parts of the dielectric function can be obtained accurately from the ellipsometric angles $\psi(\omega)$ and $\Delta(\omega)$ extracted from the optical spectra, without the need of a Kramers-Kronig analysis.

The Raman data were collected in backscattering geometry using a Dilor XY-triple grating Raman spectrometer equipped with a charge coupled device camera as detector. With power of 0.2 mW at 632 nm it was possible to measure Raman spectra on polished surfaces of the Ag_2BiO_3 samples. Low temperature Raman measurements were performed between 10-300 K. The resolution of our spectrometers for this experiment was about

3 cm^{-1} .

III. COMPUTATIONAL DETAILS

The band structure calculations for Ag_2BiO_3 presented in Fig. 3 (d) were obtained using the Vienna ab initio Simulation Package (VASP 5.4) with the generalized gradient approximation (GGA) of Perdew-Burke-Ernzerhof (PBE) type exchange-correlation potential [16]. The cutoff energy of plane wave basis set was set to be the ENMAX value in the pseudo-potential plus 30%. A-centered $3 \times 3 \times 2$ Monkhorst-Pack grid was used for the self-consistent field (SCF) calculations.

The electronic structure calculations shown in Figs. 4 (a)-(d) were performed using density functional theory (DFT) with the full-potential linearized-augmented-plane-wave code WIEN2k [17]. Exchange and correlation effects were treated within the local density approximation (LDA) [18]. For Ag_2BiO_3 , we use the $Pnn2$ unit cell with the lattice constants $a = 5.983 \text{ \AA}$, $b = 6.324 \text{ \AA}$, and $c = 9.576 \text{ \AA}$, as determined in Ref. [10]. For BaBiO_3 , we use the $P2_1/n$ unit cell with the lattice constants $a = 6.174 \text{ \AA}$, $b = 6.125 \text{ \AA}$, and $c = 8.652 \text{ \AA}$, as determined in Ref. [19]. For both bismuthates, a $6 \times 6 \times 4$ \mathbf{k} -point grid was used for the Brillouin-zone integration. Projections onto oxygen molecular orbitals were performed with a modified version of WIEN2k, following the procedure outlined in Ref. [20].

IV. RESULTS AND DISCUSSION

A. Analysis of XRD, XPS, and XAS

We used XRD, XPS and XAS measurements to demonstrate that Ag_2BiO_3 in the $Pnn2$ phase is a bond-disproportionated bismuthate. As it is difficult to distinguish the $Pnna$ structure from the $Pnn2$ structure with only PXRD data, as demonstrated in Fig. 1, we will start by accepting the reported $Pnn2$ phase reported and assess the consistency of various properties we measure with this structure. The lower scattering power of oxygen in X-ray diffraction and natural twinning of Ag_2BiO_3 crystals makes it difficult to discern the $Pnn2$ from the $Pnna$ structure. A previous powder neutron diffraction study, which is more sensitive to diffraction from oxygen than X-rays, on Ag_2BiO_3 resulted in a precise refinement of O atomic positions and a structure where Bi has two distinct sites [10]. We compare the simulated powder XRD and neutron diffraction patterns in Sup. Fig. 1 to demonstrate how the $Pnn2$ phase can be identified in neutron diffraction [21].

In the $Pnn2$ phase, Ag_2BiO_3 has two distinct bismuth sites resulting in two BiO_6 octahedra with shorter and longer Bi-O bonds. It should be emphasized that the Bi-O distances vary within each of the two types of octahedra in Ag_2BiO_3 . These BiO_6 octahedra are edge-sharing along the a direction, but only share corners along the b and c directions. The O-O distances at the shared edges of these octahedra are shorter than the distances between the other oxygen atoms, which may correspond to oxygen dimerization at the shared edges. The Ag atoms are sitting between the BiO_6 octahedra channels and are bonded to 3 oxygen atoms each. The shortest Ag-O distances for both Ag sites are 2.1464 and 2.2065 Å, which are expected for Ag^{1+} typically seen in oxides.

The X-ray photoelectron spectra for Ag, Bi, and O in Ag_2BiO_3 are presented in Figs. 2(a)-(c). As expected, only one state is observed for Ag, with peak centers at 373.8 eV (peak D1 in Fig. 2(b)) and 367.8 eV (peak D2 in Fig. 2(b)) which match the transition seen in Ag^{1+} in other oxides and chalcogenides [15]. The splitting here is expected for the d -states due to spin-orbit-coupling (SOC). The XPS of O shows three peaks at 529.1 eV (C), 530.8 eV (B), and 532.6 eV (A). As for the minor peak at 532.6 eV (peak A in Fig. 2(a)), it was attributed to surface contaminants in other bismuthates [22], and such contaminants may be present on the surface of our samples. The binding energy of the main peak for O $1s$ at 529.1 eV (peak C in Fig. 2(a)) is comparable to the binding energy of O $1s$ in BaBiO_3 [22]. XPS shows evidence for KOH on the surface of the sample as evidenced by an observed K peak (shown in Sup. Fig. 2(a)); we cannot rule out that some of the intensity at at 530.8 eV originates from KOH [23](peak B in Fig. 2(a)). Furthermore, contamination like carbonates, which were also observed in the C $1s$ spectrum (see Sup. Fig. 2(a)) might also contribute the peak B. However, analyzing the rela-

tive amount of potassium and carbonate contaminations peak B cannot be purely due to those contaminations, see Sup. Table I. Considering, that the area of the fitted curve at 530.8 eV is comparable to the area of the main peak at 529.1 eV (Table I in SI), we expect the signal to originate from a similar amount of oxygen atoms on the surface of the Ag_2BiO_3 samples. Looking at the different O-O and Bi-O distance for oxygen atoms at the shared edges and corners of the BiO_6 octahedra, we propose that the peaks at 530.8 eV and 529.1 eV may originate from different states in the oxygen atoms at the shared corners and the shared edges of the BiO_6 octahedra.

Assigning distinct oxygen atoms as the origin for the different XPS peaks, the peak at 529.1 eV may originate from the dimerized oxygen at the shared edges of the octahedra with a bond length of 2.6588 Å, while the contribution to the peak at 530.8 eV from Ag_2BiO_3 likely comes from the corner shared oxygens. Another possibility is that the different oxygen states at 529.1 and 530.8 eV arise from the interaction of the oxygen atoms with silver atoms at different distances, where the oxygen atoms at the shared corners of the octahedra are further away from the nearest silver atoms, while the oxygen atoms at the shared edges are closer to silver atoms. If all oxygen atoms in Ag_2BiO_3 have equivalent Bi-O interaction, then the electronic origin for the split peaks at 529.1 and 530.8 eV depends on the extent of the O $1s$ core-hole potential and the Bi $6s/\text{O } 2p$ hybridization [22].

The Bi $4f$ spectra, shown in Fig. 2(c), support the presence of two Bi states in this compound, and these states have similar binding energy (158.0 eV for peak G2 and 158.5 eV for peak F2). The ratio of the areas of the two peaks is nearly 1:1, suggesting that the two different Bi states are due to the two distinct Bi atoms in the unit cell. It might be possible that one of the Bi states is due to surface contaminations like hydroxides or carbonates. However, this would imply that the 1:1 ratio of the two Bi states observed is mere coincidence. Furthermore, if one of the components would be due to contamination the amount of Bi would be too little compared to the Ag amount (see Table I in SI). For now, we consider the two Bi peaks observed as originating from Ag_2BiO_3 . Comparing the measured binding energies with those for Bi^{5+} like in NaBiO_3 [24] and Bi^{3+} like in Bi_2O_3 [11] we realize that both are close to the value for Bi^{3+} . This might hint that the system is bond disproportionated rather than charge disproportionated. Please note that the Bi $4f$ binding energies are similar to the one observed in BaBiO_3 [25] but the Bi $4f$ spectrum for Ag_2BiO_3 shows a clearer asymmetry.

The XPS spectra thus indicate two different Bi sites, consistent with a disproportionated state, and optical conductivity evidence for a band gap (Section IV B) support this interpretation. However, whether Ag_2BiO_3 is charge or bond disproportionated remains unclear without examining the XAS data. XAS results at the oxygen K -edge, presented in Fig. 3(a), show a sharp pre-peak at 529 eV, which originates from a high hole density in

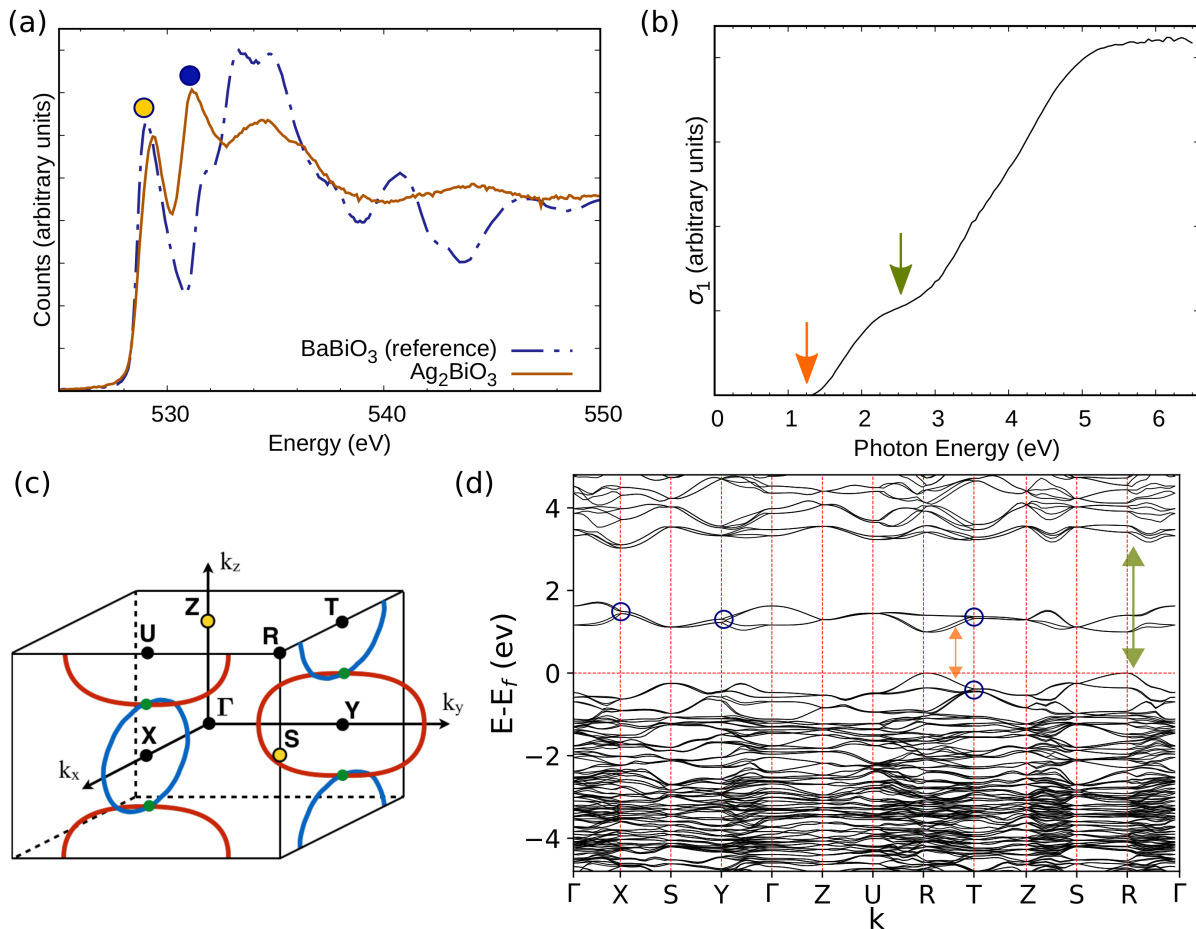


FIG. 3: (a) The X-ray absorption spectra at the Oxygen K -edge of Ag_2BiO_3 and a reference sample of BaBiO_3 . (b) Optical spectroscopy data on Ag_2BiO_3 extracted from ellipsometry measurement. (c) Brillouin zone of Ag_2BiO_3 with the high-symmetry points indicated by black dots. The nodal chains are schematically illustrated by the blue and red lines. At the Z and S points (yellow) there are fourfold degeneracies, formed by two Weyl points with opposite chirality. (d) Band structure of Ag_2BiO_3 in the $Pnn2$ phase using DFT calculation with hybrid functionals.

the oxygen p orbitals. This is similar to the results on BaBiO_3 [22]. The higher energy region at the K -edge is clearly different from the BaBiO_3 spectrum, reflecting the different oxygen environment in Ag_2BiO_3 . A second peak is seen in the XAS results of Ag_2BiO_3 , and the two XAS peaks (marked with yellow and blue circles in Fig. 3(a)) are ~ 2 eV apart. This energy difference is similar to peaks B and C in the oxygen XPS spectra.

The combination of corner and edge sharing octahedra in Ag_2BiO_3 can contribute to the different XAS spectra above 530 eV. Another peak at 531 eV is seen for Ag_2BiO_3 , and the origin of this peak is the higher energy states of O in Ag_2BiO_3 . If we compare Figs. 4(c) and (d), we see a peak in the oxygen partial density of states at 2 eV in Ag_2BiO_3 that is much less intense than in BaBiO_3 . In the ionic-limit, we have $\text{Ag}^{1+}4d^{10}$, $\text{Bi}^{3+}6s^2$, and $\text{O}^{2-}2p^6$ ions making up Ag_2BiO_3 , where the BiO_6 octahedra are either made up of $\text{Bi}^{3+}(6s^2)\text{-O}$ bonds with longer bonds or $\text{Bi}^{3+}(6s^2\bar{L}^2)\text{-O}$ with shorter bonds. The ligand hole pairs (\bar{L}^2) condense on these smaller octahe-

dra, where the O atoms have equal charge on them. The disproportionation leading to the small and large octahedra in this case is described as bond-disproportionation.

One is tempted to conclude a similar origin for both of these sets of peaks, such as the difference between oxygen atoms at the shared edges and corners of the BiO_6 octahedra. However, the area under the curve for the XPS peaks is equivalent for B and C. Reconciling the XAS and XPS results, if the oxygen atoms are equivalent in terms of interaction with Bi and the split in the O 1s XPS is electronic in nature, then an oxygen ligand hole will be distributed over 6 oxygen atoms in the BiO_6 octahedron. In the case of O 1s, the XPS peak splitting originates from oxygen atoms at different distances to bismuth, which suggests an oxygen hole may be distributed over 4 oxygen atoms at the shared edges of the BiO_6 octahedra. The oxygen hole ligand distribution in the octahedra of Ag_2BiO_3 is discussed below in section IV C.

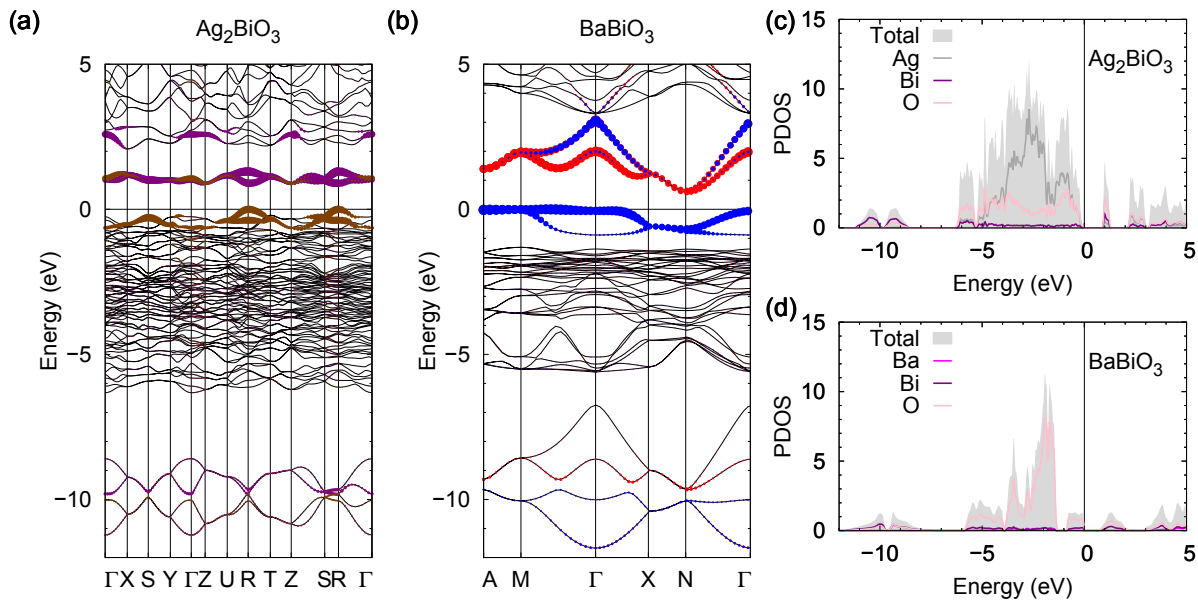


FIG. 4: (a) The DFT (LDA) band structures of Ag₂BiO₃ in the *Pnn2* phase. The contribution from the O-*a*_{1g} molecular orbital of the small (purple) and large (brown) octahedra are represented with fat bands. The colors for octahedra are matching the Ag₂BiO₃ unit cell presented in Fig. 1(c). (b) The band structures of BaBiO₃ in the *P2*₁/*n* phase. The contribution from the O-*a*_{1g} molecular orbital of the small (red) and large (blue) octahedra are represented with fat bands. The colors for octahedra are matching the BaBiO₃ unit cell presented in Fig. 1(e). (c) Partial Density of States (PDOS) of Ag₂BiO₃, showing the contribution from Ag, Bi, and O. (d) PDOS of BaBiO₃, showing the contribution of Ba, Bi, and O.

B. Band Gap and Topology in Disproportionated Ag₂BiO₃

The band structure of Ag₂BiO₃ in the *Pnn2* phase resulting from DFT calculations is presented in Fig. 3(d), where we have a band gap of ~ 1.25 eV resulting from hybridization of O 2*p* bands and Bi 6*s* band, with antibonding character. The second set of bands above the Fermi level (E_F) is located ~ 3 eV above E_F and corresponds to the unfilled Bi 6*p* bands. The band gap from optical conductivity measurement is around ~ 1.25 eV (Fig. 3(b)), transition between bands marked with an orange arrow, which corresponds well with transitions expected in our calculated band structure, marked with an orange arrow in Fig. 3(d). The real and imaginary parts of the dielectric constant of Ag₂BiO₃ are shown in Sup. Fig. 3. The upturn starting at ~ 2.5 eV in the optical conductivity corresponds to transitions from bands below E_F to the empty Bi 6*p* bands in Ag₂BiO₃, which are marked with green arrows in Figs. 3(b) and (d). The consistency between the features seen in our optical conductivity measurement and the expected transitions in our calculated band structure provide further evidence for Ag₂BiO₃ being in the disproportionated *Pnn2* phase. In the *Pnna* phase Ag₂BiO₃ is a semimetal and expected to have a nonzero density of state at the Fermi level [6], so no gap in the optical conductivity.

We emphasize that the non-symmorphic space group *Pnn2* (Space Group 34) of Ag₂BiO₃ leads to symmetry-enforced nodal loops in all bands, i.e., twofold Weyl cross-

ings along 1D loops. These nodal loops are protected by the glide mirror symmetries $\{m_{010}|\frac{1}{2}\frac{1}{2}\frac{1}{2}\}$ and $\{m_{100}|\frac{1}{2}\frac{1}{2}\frac{1}{2}\}$ and touch each other on the intersection lines of the mirror planes, thereby forming “nodal chains” [26–28], see Fig. 3(c). These Weyl nodal lines carry a nontrivial π -Berry phase, leading to drumhead surface states. The Weyl nodal-chain feature is not removable by perturbations as long as the glide mirror symmetries are preserved. In our band calculations of Fig. 3(d) these Weyl nodal chains are seen in various bands as crossing points close to high-symmetry points (see, e.g. crossings marked by blue circles close to the X, Y, and T points). To access the anomalous magnetotransport properties of the nodal chains [26], we may be tempted to use chemical doping to shift the Fermi level and approach these band crossings. However, if the chemical doping changes the *Pnn2* symmetry, then these topological features may be annihilated. In addition, we note that at the S and Z points the bands form fourfold degeneracies, composed of two Weyl points with opposite chirality (yellow dots in Fig. 3(c)).

Including hybrid functionals in our calculations results in an increase in the band gap for Ag₂BiO₃ in comparison with calculations in the literature [6] with a direct gap of ~ 1.0 eV at the *R* point in the band structure. However, this value remains slightly lower than the experimentally estimated value of ~ 1.25 eV from our optical conductivity measurement. This may be limited by the optically active transitions in Ag₂BiO₃ that do not correspond to the lowest band gap in our band structure, or the in-

adequacy of the band calculations in providing accurate band gap values even with hybrid functionals. Ag_2BiO_3 in the $Pnn2$ is predicted to be a good photovoltaic material [29], and our results clarifying the band gap experimentally are an important step forward. The ~ 1.25 eV band gap in Ag_2BiO_3 falls within 1.1-1.45 eV range where maximum efficiency is expected for single junction solar cells [30]. XPS results, shown in Sup. Fig. 2(b), suggest the valence band is ~ 0.9 eV below the Fermi level, and this shows promise for introducing in-gap-states in Ag_2BiO_3 . In future studies, we will need to examine the stability of Ag_2BiO_3 when exposed to different radiation to assess its potential in photovoltaic applications.

C. Comparing Ag_2BiO_3 and BaBiO_3

Next, we would like to highlight the extent of similarity and some of the differences between Ag_2BiO_3 and BaBiO_3 . Both materials have a bulk band gap due to disproportionation of “ Bi^{4+} ”, but the octahedra are only corner sharing in BaBiO_3 while the octahedra are sharing edges and corners in Ag_2BiO_3 . The nominal Bi^{4+} oxidation state that leads to the disproportionated charge/bonds in these compounds is achieved through a different number of atoms. While having one Bi atom and three oxygen atoms, it takes two monovalent Ag^{1+} ions or one divalent Ba^{2+} ion to achieve the same average formal charge of $4+$ for Bi. Thus, $(\text{Ag}^{1+})_2(\text{Bi}^{4+})(\text{O}^{2-})_3$ and $(\text{Ba}^{2+})(\text{Bi}^{4+})(\text{O}^{2-})_3$ have the same unstable average formal charge for Bi in different crystal structures, and lead to disproportionation in both Ag_2BiO_3 and BaBiO_3 . However, similar to BaBiO_3 , there is a significant amount of oxygen character in the empty conduction states of Ag_2BiO_3 above the Fermi level. To be more specific, these states are formed by oxygen molecular orbitals with a_{1g} symmetry centered on the *small* BiO_6 octahedra. In Fig. 4 (a), they are highlighted as purple fat bands for Ag_2BiO_3 , while in Fig. 4 (b), they are highlighted as red fat bands for BaBiO_3 . In the previous theoretical studies on BaBiO_3 [31, 32], this situation was referred to as a bi-polaronic condensation of oxygen holes. For Ag_2BiO_3 we show in Sup. Fig. 4 the orbital contribution from Bi-*s* and *p* in the small and large O_6 octahedral cages, as well as the $\text{O}-2p$. The significant contribution of $\text{O}-2p$ above the Fermi level is consistent with high density of oxygen holes as evidenced by the pre-peak in XAS (Fig. 3(a)).

As one can also see in Fig. 4, the valence state within ~ 1 eV range below the Fermi level has, in turn, a strong character of $\text{O}-a_{1g}$ molecular orbitals centered on the *large* BiO_6 octahedra (brown fat bands for Ag_2BiO_3 and blue fat bands for BaBiO_3). Together, these two sets of oxygen molecular orbital states around the Fermi level constitute the anti-bonding manifold resulting from the strong hybridization between the Bi- $6s$ and $\text{O}-a_{1g}$ orbitals. The latter appears to be as strong in Ag_2BiO_3 as it was found to be in BaBiO_3 , which is evident from the fact that in both systems the bonding combination

is pushed down as far as -10 eV. A new feature of the Ag_2BiO_3 band-structure is the presence of Ag- $4d$ bands in the same energy region where the non-bonding oxygen bands are located, from ~ -7 eV up to the Fermi level (Shown in Sup. Fig. 4(a)). It was demonstrated in BaBiO_3 that the octahedral angle between BiO_6 octahedra affects the Bi-O hybridization [32]. Band calculations in BaBiO_3 with a 0° and 16° octahedral tilting show bands with narrower energy dispersion with increased tilt angle. The conduction band in Ag_2BiO_3 is considerably narrower compared to that in BaBiO_3 , which is probably a result of weaker Bi-O hybridization due to the geometrical arrangement of the BiO_6 octahedra in Ag_2BiO_3 . In Ag_2BiO_3 , the edge-sharing BiO_6 octahedra along the *a* direction, and the high angle of 36° between the Bi-O-Bi at the shared corners along the *b* and *c* directions contribute to reduced hybridization. This qualitative statement about the hybridization should be confirmed with DFT calculations in future studies. The Ag might play a role in reducing the band gap in Ag_2BiO_3 , as seen in the Ag-containing pyrochlore oxides [33]. This narrowing effect is not clear when we compare Ag_2BiO_3 with BaBiO_3 due to the different crystal structure, but replacing the Ag with another monovalent atom, such as Na_2BiO_3 , can help us to study the effect of Ag. The contribution from Ag bands near the Fermi level is shown in the partial density of states (PDOS) of Ag_2BiO_3 presented in Fig. 4(c). In comparison, the PDOS of BaBiO_3 , shown in Fig. 4(d), has significant contribution from only Bi and O near the Fermi level and no significant contribution from the Ba.

While in BaBiO_3 we have an indirect band gap as shown in Fig. 4 (b), in Ag_2BiO_3 the band gap is direct as shown in Fig 3(d) and Fig. 4 (a). The role of the Ag- $4d$ bands that extend over a wide energy range below the Fermi level is not clear for now. Identifying the effect of edge sharing BiO_6 octahedra, crystal symmetry, and Ag bands on the band structure of Ag_2BiO_3 will be an important part of future studies. Future work should include replacing Ag with other monovalent metal M^{+1} atoms, varying tilting angle of BiO_6 octahedra, and studying the lower symmetry Pn phase.

The Raman spectra of Ag_2BiO_3 have a strong phonon mode at 520 cm^{-1} , shown in Fig. 5, which is similar to the phonon mode observed in pristine BaBiO_3 at 570 cm^{-1} [34]. In the case of BaBiO_3 , the phonon is attributed to the breathing mode originating from local distortion in the bond disproportionated BaBiO_3 , so it is likely that a similar energy phonon originates from a similar breathing mode accompanying the disproportionation in Ag_2BiO_3 . The slight difference in energies between the phonon modes in Ag_2BiO_3 and BaBiO_3 is due to the different arrangement of the BiO_6 octahedra in the two compounds and the slightly different Bi-O distances. A higher energy phonon mode originating from higher harmonic phonon modes can be seen in the Raman spectra of Ag_2BiO_3 at 1100 cm^{-1} , which is similar in value to phonons in the spectra of pristine BaBiO_3 [34].

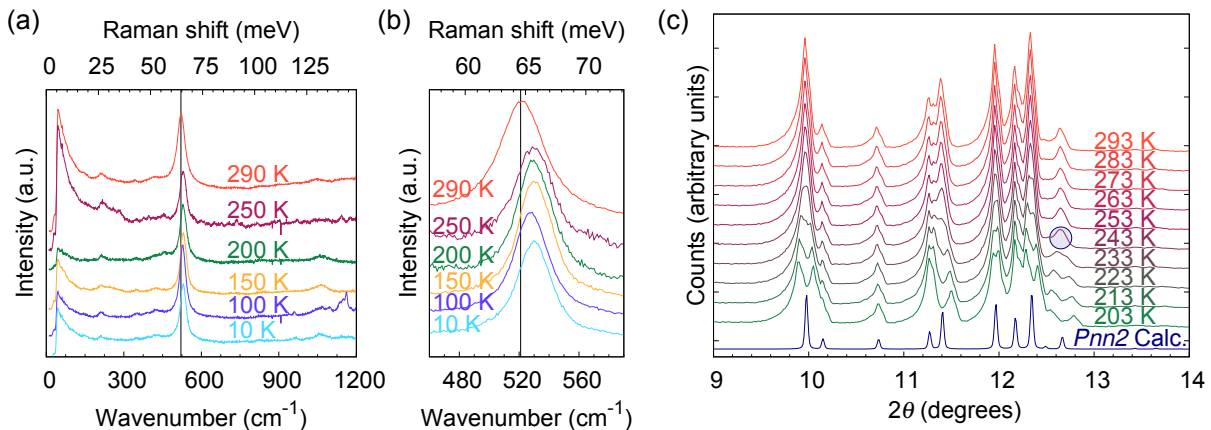


FIG. 5: (a) Raman spectra of Ag_2BiO_3 at different T , between 290–10 K. (b) The same Raman spectra in (a), emphasizing the peak at 520 cm^{-1} , characteristic of the breathing mode in disproportionated bismuthates. (c) Powder-XRD of Ag_2BiO_3 collected at different T , between 293–203 K. The calculated XRD pattern for Ag_2BiO_3 in the $Pnn2$ phase is plotted at the bottom.

D. Transition to Pn Phase in Ag_2BiO_3

We have closely measured the phonon mode at 520 cm^{-1} as a function of temperature between 290 K and 10 K, and have observed a shift in the phonon peak position cooling down from 290 K to 250 K, but no further shift in the phonon mode cooling down to 10 K. We have performed powder XRD measurements on Ag_2BiO_3 at low T and observe a splitting in some peaks at 240 K that corresponds to the monoclinic distortion previously reported [10]. This distortion leads to reduction of symmetry of Ag_2BiO_3 from $Pnn2$ to Pn .

As explained in Sec. IV A, it is difficult to distinguish whether Ag_2BiO_3 crystallizes in the $Pnn2$ or the $Pnna$ phase from XRD alone, and neutron diffraction studies were required to clarify the $Pnn2$ phase at room temperature [10]. The band gap and splitting in the Bi XPS states measured on our samples suggest that Ag_2BiO_3 is indeed in the $Pnn2$ phase. However, the Pn phase of Ag_2BiO_3 is distinct from the higher symmetry phases and can be identified with XRD. The splitting of the (202) peak at $\sim 12.6^\circ$ for temperatures $< 243\text{ K}$ is highlighted with a blue circle in Fig. 5(c), which results from the reduced symmetry of Ag_2BiO_3 $Pnn2$ to Pn .

It is likely that the shift in the phonon mode observed in Raman measurements at 250 K is related to the phase transition observed in powder XRD. The transition observed in our samples is consistent with the previously reported phase transition in neutron diffraction measurements on Ag_2BiO_3 [10]. In future studies, we hope to investigate the effect of different synthesis conditions on the oxygen content in Ag_2BiO_3 , and whether this influences the distortion in these samples at low T .

Measurements that can be used to probe the band structure of Ag_2BiO_3 such as scanning tunneling spectroscopy or angle-resolved photoemission spectroscopy are typically performed at low temperature. Any prop-

erties measured on Ag_2BiO_3 below $\sim 250\text{ K}$ are representative of the material in the Pn phase, and the band structure of this phase will be the relevant one for those measurements. Luckily, the Pn (Space Group 7) symmetry falls into the non-symmorphic space groups where a single glide mirror symmetry is expected to lead to symmetry-enforced Weyl nodal lines [26–28], albeit not a nodal chain as in the $Pnn2$ phase.

The disproportionation of Ag_2BiO_3 is still prevalent in the Pn phase, which would lead to a band gap much like the $Pnn2$ phase. Repeating the XPS and XAS measurements at temperatures where Ag_2BiO_3 is in the Pn phase will help reveal whether this transition affects the Bi states or the oxygen holes.

V. CONCLUSIONS

We have demonstrated that despite the use of a high pressure of 6 GPa, Ag_2BiO_3 samples crystallize in a structure consistent with the $Pnn2$ phase as evidenced by the XPS data for Bi and the measured band gap. The band gap observed in our study is consistent with our band calculations, and we demonstrate that Ag_2BiO_3 even in the $Pnn2$ phase is topologically non-trivial and contains Weyl-nodal chains in its band structure ($\sim 0.5\text{ eV}$ below the Fermi level). We observe a phase transition in Ag_2BiO_3 at low temperatures associated with distortion from the $Pnn2$ phase to the Pn phase from our XRD pattern and Raman spectra. Even in the Pn phase Ag_2BiO_3 falls into a non-symmorphic space group and Weyl nodal-line features are expected.

The XAS spectra of Ag_2BiO_3 suggests the presence of oxygen holes much like BaBiO_3 , which is consistent with Ag_2BiO_3 being a bond disproportionated bismuthate. Despite the different arrangement of BiO_6 octahedra in BaBiO_3 and Ag_2BiO_3 , we observe a phonon mode in the Raman spectra of Ag_2BiO_3 at similar energy associated

with breathing mode of the disproportionated BaBiO_3 . Our results push forward the group of monovalent bismuthates $(M^{+1})_2\text{BiO}_3$ as a new class of bismuthates with novel topological properties. Doping of divalent atoms on the Ag-site and performing in-situ high-pressure experiments may allow us to destabilize the disproportionation in Ag_2BiO_3 , and achieve a metallic state and perhaps even superconductivity in this class of materials in analogy to BaBiO_3 . We envision that this work will open up the field of disproportionated oxides beyond those in the perovskite structure.

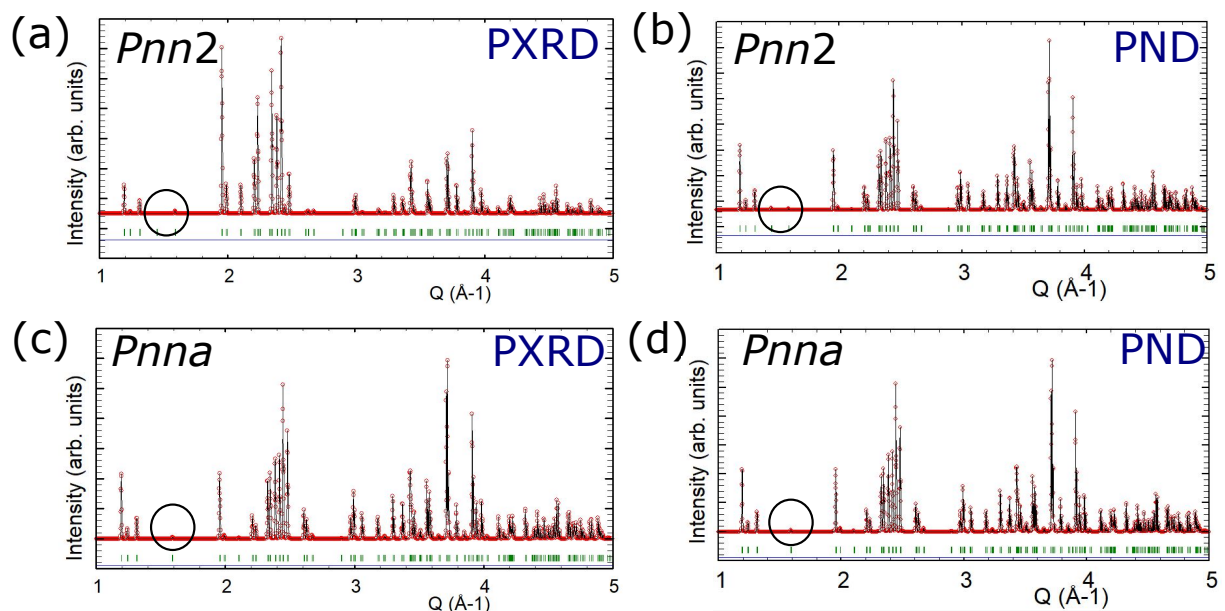
VI. ACKNOWLEDGEMENTS

We thank Frank Falkenberg, Christine Stefani, Sebastian Bette, and Armin Schulz for technical assistance

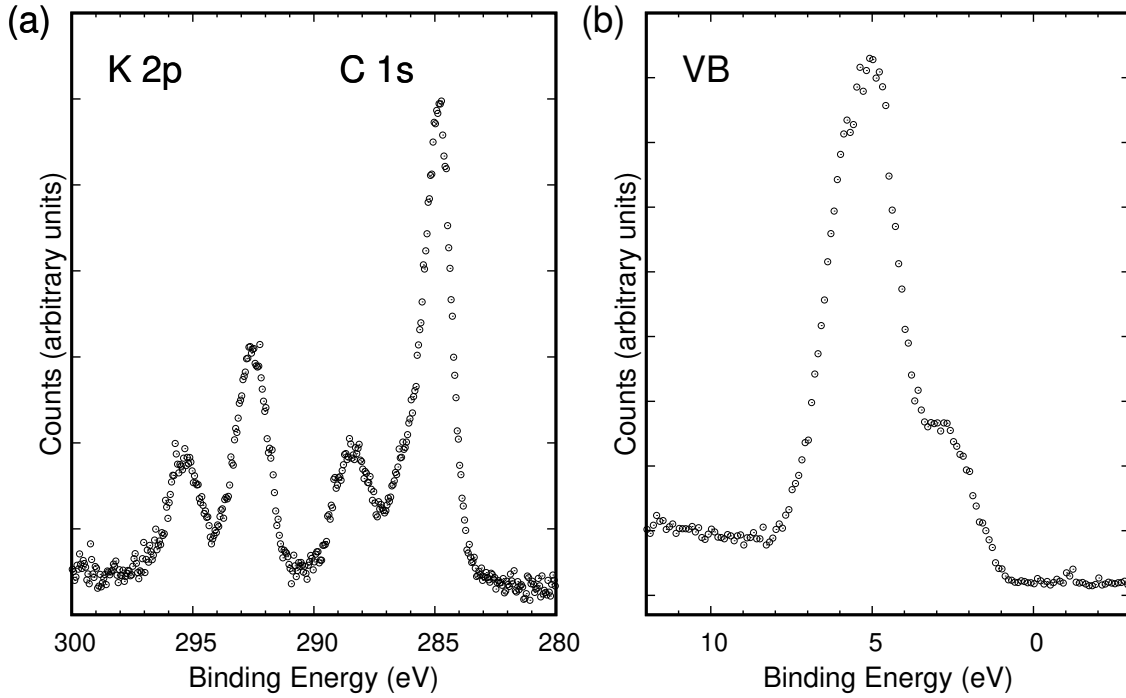
with experiments. We thank Tom Regier for help with XAS measurements. Research described in this paper was performed at the Canadian Light Source, which is supported by the Canada Foundation for Innovation, Natural Sciences and Engineering Research Council of Canada, the University of Saskatchewan, the Government of Saskatchewan, Western Economic Diversification Canada, the National Research Council Canada, and the Canadian Institutes of Health Research. We thank the Max Planck-UBC-UTokyo Center for Quantum Materials for support.

-
- [1] J. G. Bednorz and K. A. Müller, *Z. Phys. B* **64**, 189 (1986).
- [2] L. Mattheiss, E. Gyorgy, and D. Johnson Jr, *Phys. Rev. B* **37**, 3745 (1988).
- [3] S. Seki, X. Yu, S. Ishiwata, and Y. Tokura, *Science* **336**, 198 (2012).
- [4] M. Kargarian and G. A. Fiete, *Phys. Rev. Lett.* **110**, 156403 (2013).
- [5] S. Ishiwata, T. Nakajima, J.-H. Kim, D. Inosov, N. Kanazawa, J. White, J. Gavilano, R. Georgii, K. Seemann, G. Brandl, et al., *Phys. Rev. B* **101**, 134406 (2020).
- [6] J. He, D. Di Sante, R. Li, X.-Q. Chen, J. M. Rondinelli, and C. Franchini, *Nat. Commun.* **9**, 492 (2018).
- [7] B. Fu, X. Fan, D. Ma, C.-C. Liu, and Y. Yao, *Phys. Rev. B* **98**, 075146 (2018).
- [8] B. Singh, B. Ghosh, C. Su, H. Lin, A. Agarwal, and A. Bansil, *Phys. Rev. Lett.* **121**, 226401 (2018).
- [9] S. Deibele and M. Jansen, *J. Solid State Chem.* **147**, 117 (1999).
- [10] C. P. Oberndorfer, R. E. Dinnebier, R. M. Ibberson, and M. Jansen, *Solid State Sci.* **8**, 267 (2006).
- [11] M. Hegde, P. Barboux, C. Chang, J. Tarascon, T. Venkatesan, X. Wu, and A. Inam, *Phys. Rev. B* **39**, 4752 (1989).
- [12] N. Quackenbush, J. W. Tashman, J. A. Mundy, S. Sallis, H. Paik, R. Misra, J. A. Moyer, J.-H. Guo, D. A. Fischer, J. C. Woicik, et al., *Nano Lett.* **13**, 4857 (2013).
- [13] P. Swift, *Surf. Interface Anal.* **4**, 47 (1982).
- [14] T. L. Barr and S. Seal, *J. Vac. Sci. Technol. A* **13**, 1239 (1995).
- [15] J. Moulder and J. Chastain, *Handbook of X-ray Photoelectron Spectroscopy: A Reference Book of Standard Spectra for Identification and Interpretation of XPS Data* (Physical Electronics Division, Perkin-Elmer Corporation, 1992).
- [16] J. P. Perdew, K. Burke, and Y. Wang, *Phys. Rev. B* **54**, 16533 (1996).
- [17] P. Blaha, K. Schwarz, G. K. Madsen, D. Kvasnicka, and J. Luitz, An augmented plane wave+ local orbitals program for calculating crystal properties (2001).
- [18] J. P. Perdew and Y. Wang, *Phys. Rev. B* **45**, 13244 (1992).
- [19] B. J. Kennedy, C. J. Howard, K. S. Knight, Z. Zhang, and Q. Zhou, *Acta Crystallogr. B* **62**, 537 (2006).
- [20] K. Foyevtsova and G. Sawatzky, *J. Mod. Phys.* **10**, 953 (2019).
- [21] See Supplemental Material for further detail..
- [22] S. Balandeh, R. J. Green, K. Foyevtsova, S. Chi, O. Foyevtsov, F. Li, and G. A. Sawatzky, *Phys. Rev. B* **96**, 165127 (2017).
- [23] M. Favaro, B. Jeong, P. N. Ross, J. Yano, Z. Hussain, Z. Liu, and E. J. Crumlin, *Nat. Commun.* **7**, 12695 (2016).
- [24] G. Kulkarni, V. Vijayakrishnan, G. Ranga Rao, R. Seshadri, and C. Rao, *Appl. Phys. Lett.* **57**, 1823 (1990).
- [25] N. Plumb, D. Gawryluk, Y. Wang, Z. Ristić, J. Park, B. Lv, Z. Wang, C. Matt, N. Xu, T. Shang, et al., *Phys. Rev. Lett.* **117**, 037002 (2016).
- [26] T. Bzdušek, Q. Wu, A. Rüegg, M. Sigrist, and A. A. Soluyanov, *Nature* **538**, 75 (2016).
- [27] Y.-H. Chan, B. Kilic, M. M. Hirschmann, C.-K. Chiu, L. M. Schoop, D. G. Joshi, and A. P. Schnyder, *Phys. Rev. Mater.* **3**, 124204 (2019).
- [28] M. M. Hirschmann, A. Leonhardt, B. Kilic, D. H. Fabini, and A. P. Schnyder, *Symmetry-enforced band crossings in tetragonal materials: Dirac and weyl degeneracies on points, lines, and planes* (2021), 2102.04134.
- [29] D. H. Fabini, M. Koerner, and R. Seshadri, *Chem. Mater.* **31**, 1561 (2019).
- [30] T. Kirchartz and U. Rau, *Adv. Energy Mater.* **8**, 1703385 (2018).
- [31] K. Foyevtsova, A. Khazraie, I. Elfimov, and G. A. Sawatzky, *Phys. Rev. B* **91**, 121114 (2015).
- [32] A. Khazraie, K. Foyevtsova, I. Elfimov, and G. A. Sawatzky, *Phys. Rev. B* **97**, 075103 (2018).
- [33] H. Mizoguchi and P. M. Woodward, *Chem. Mater.* **16**, 5233 (2004).
- [34] S. Tajima, M. Yoshida, N. Koshizuka, H. Sato, and S. Uchida, *Phys. Rev. B* **46**, 1232 (1992).

Electronic Structure of the Bond Disproportionated Bismuthate Ag_2BiO_3 - Supplemental Material



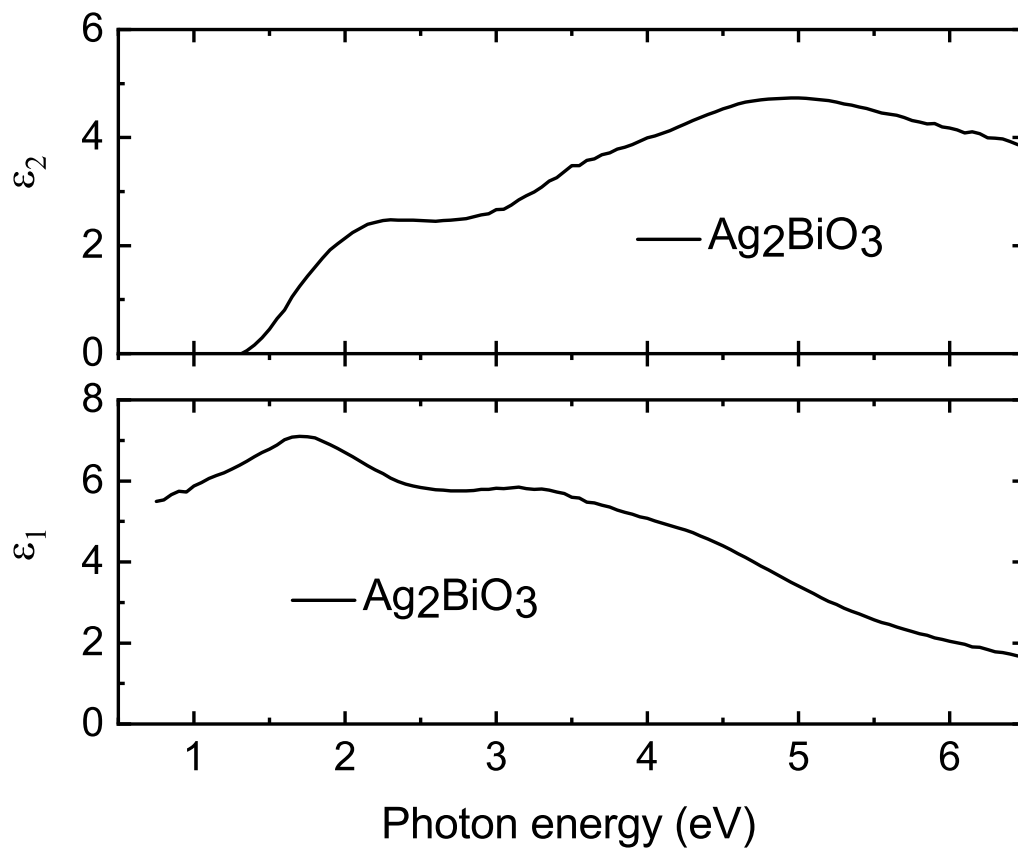
Supplementary Figure 1: Powder X-ray diffraction (PXR) and powder neutron diffraction (PND) simulation Ag_2BiO_3 in the *Pnn2* phase shown in (a) and (b), respectively. PXR and PND simulation of Ag_2BiO_3 in the *Pnna* phase shown in (c) and (d), respectively. Diffraction patterns are plotted as a function of the reciprocal lattice vector (Q). Black circles in the figures highlight one of the peaks only observable in the PND for the *Pnn2* phase.



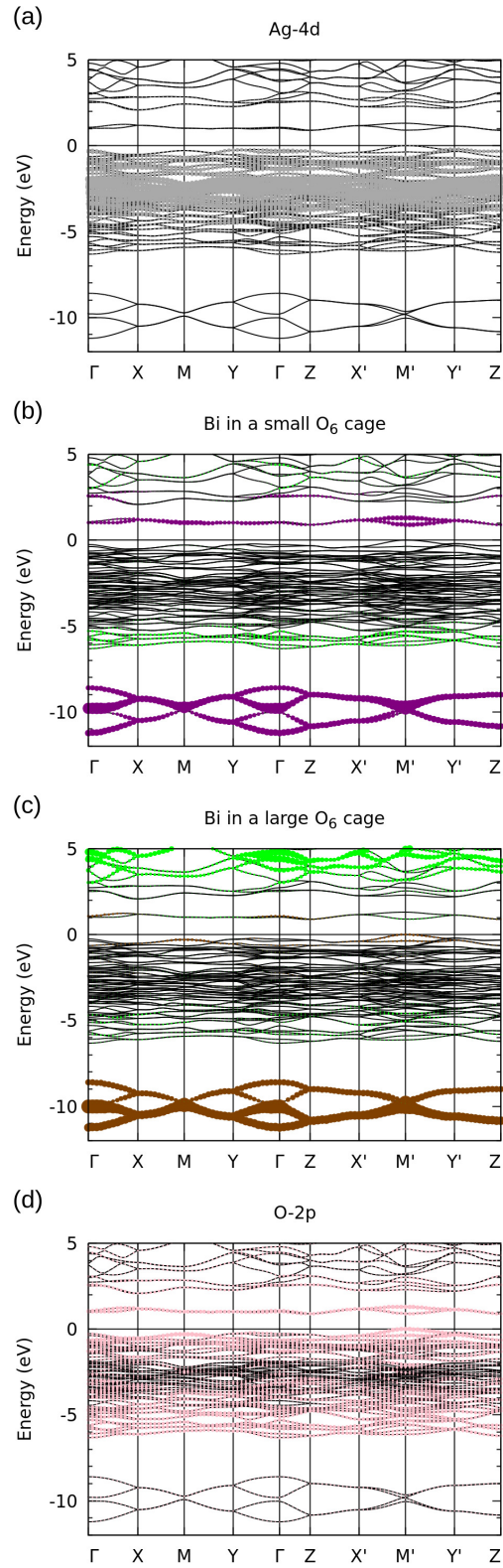
Supplementary Figure 2: X-ray photoelectron spectra of K 2p and C 1s (a) and of the valence band of Ag₂BiO₃ (b). In (b) the valence band edge is approx. 0.9 eV below the Fermi level.

Supplementary Table I: Binding energy, assignment, full width at half-maximum (FWHM) and amount of the species observed via XPS. Please note that due to surface contaminations, error in the detector function and atomic sensitivity the amount might have an error in the range of 10-15%.

element	Assignment	Binding energy [eV]	FWHM [eV]	Amount in [%]
O 1s	Ag ₂ BiO ₃ edge shared (peak C)	529.1	1.1	11.9
O 1s	Ag ₂ BiO ₃ corner shared (peak B) (small amounts of OH, carbonate contaminations)	530.8	1.7	11.8
O 1s	Water, hydroxides (peak A)	532.6	1.7	1.9
C 1s	C-C, C-H contaminations	284.8	1.5	8.4
C 1s	C-OH contaminations	285.7	2.2	6.0
C 1s	carbonate	288.5	1.7	4.0
K 2p _{3/2}	KOH	292.6	1.5	2.5
Ag 3d _{5/2}	Ag ₂ BiO ₃ (peak D2)	367.8	1.2	16.1
Bi 4f _{7/2}	Ag ₂ BiO ₃ (peak G2)	158.0	0.9	4.4
Bi 4f _{7/2}	Ag ₂ BiO ₃ (peak F2)	158.5	1.4	5.2



Supplementary Figure 3: Imaginary (ϵ_2 , top figure) and real (ϵ_1 , bottom figure) parts of the dielectric constant of Ag₂BiO₃ extracted from ellipsometry measurement.



Supplementary Figure 4: (a) The DFT (LDA) band structures of Ag_2BiO_3 in the $Pnn2$ phase with fat band representation of atomic orbital contributions. (a) The atomic orbital of the Ag-4d shown in grey fat bands. (b) The fat bands of Bi-s (green) and Bi-p (purple) contribution in the small O_6 octahedral cage. (c) The fat bands of Bi-s (green) and Bi-p (brown) contribution in the large O_6 octahedral cage. (d) The atomic orbital of the O-2p shown in pink fat bands.